

## Article

# Hierarchically Structured Stretchable Conductive Hydrogels for High-Performance Wearable Strain Sensors and Supercapacitors

Yusen Zhao, Bozhen Zhang, Bowen Yao, ..., Kareem Youssef, Qibing Pei, Ximin He

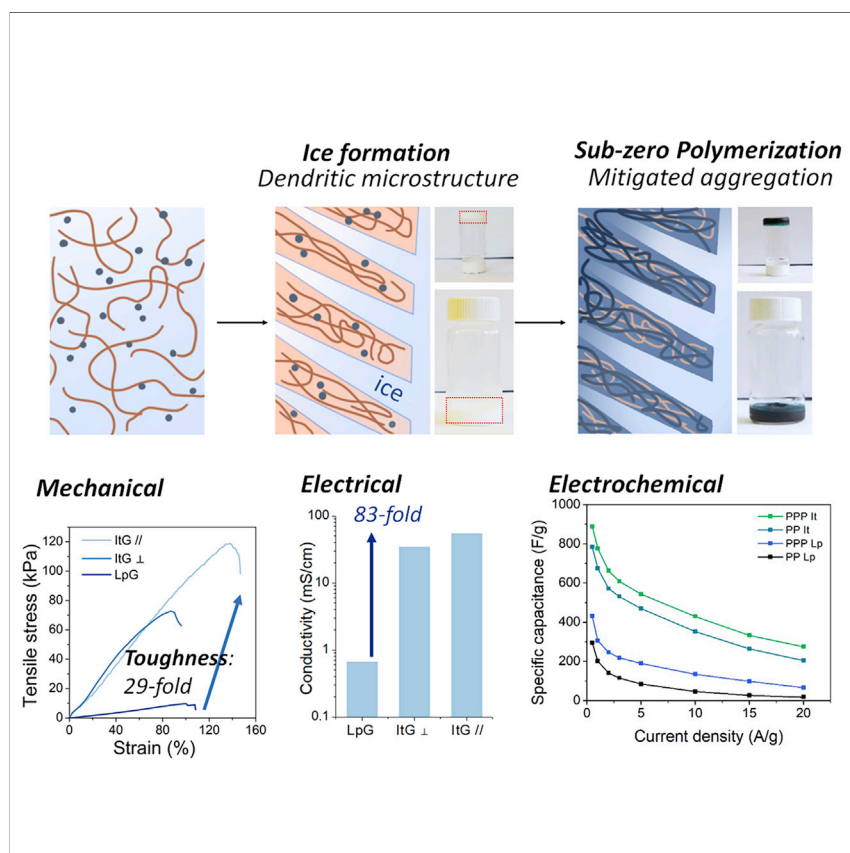
ximinhe@ucla.edu

## HIGHLIGHTS

A general-purpose method to synthesize enhanced stretchable conductive materials

Application: strain sensors with broad sensing range and high sensitivity

Application: high-capacitance stretchable solid-state supercapacitors



A strategy of creating stretchable conducting hydrogels for emerging soft electronics is reported. With ice-templated low-temperature polymerization (ITLP), the conducting gel exhibited a hierarchical dendritic microstructure with mitigated nanoaggregation and significantly enhanced electrical conductivity and toughness. Using such gels, strain sensors presented a broad sensing range and high sensitivity for health monitoring. Stretchable solid-state supercapacitors demonstrated remarkable capacitance and flexibility as wearable energy-storage devices. Such a general ITLP method may create diverse soft-electronic materials for energy, healthcare, and robotic applications.



## Improvement

Enhanced performance with innovative design or material control

Zhao et al., Matter 3, 1196–1210  
October 7, 2020 © 2020 Elsevier Inc.  
<https://doi.org/10.1016/j.matt.2020.08.024>



## Article

# Hierarchically Structured Stretchable Conductive Hydrogels for High-Performance Wearable Strain Sensors and Supercapacitors

Yusen Zhao,<sup>1,4</sup> Bozhen Zhang,<sup>2,4</sup> Bowen Yao,<sup>1</sup> Yu Qiu,<sup>1</sup> Zihang Peng,<sup>1</sup> Yucheng Zhang,<sup>1</sup> Yousif Alsaied,<sup>1</sup> Imri Frenkel,<sup>1</sup> Kareem Youssef,<sup>1</sup> Qibing Pei,<sup>1</sup> and Ximin He<sup>1,3,5,\*</sup>

## SUMMARY

Stretchable conductive materials, a critical building block of soft electronics, typically require multiple components that synergistically contribute good mechanical, electrical, and interfacial properties. The overall performance is often hindered by phase instability and poor miscibility of functional fillers within polymer matrices, compromising the conductive percolative network. We addressed this challenge with an ice-templated, low-temperature polymerization (ITLP) strategy and created stretchable conducting hydrogels. Owing to a hierarchical dendritic microstructure with mitigated nanoaggregation, the material exhibited 29-fold enhancement in toughness and 83-fold increase in conductivity. Strain sensors using such gels demonstrated a broad detection range, high sensitivity, and health-monitoring capability. ITLP gel electrodes exhibited 888 F/g specific capacitance and 2,097 mF/cm<sup>2</sup> areal capacitance (368 F/g) when used in solid-state supercapacitors. Flexible and stretchable wearable supercapacitors have been successfully made and can power LEDs. The ITLP strategy is anticipated to create diverse high-performance soft-electronic materials for broad applications in energy, healthcare, and robotics.

## INTRODUCTION

Newly developed flexible and stretchable electronics seek to bridge the gap between human and machine by either performing human functions, such as in artificial skins<sup>1</sup> and multifunctional prosthetics for assisting human movements,<sup>2</sup> or interfacing with clothing or the human body, such as in conductive interconnects,<sup>3</sup> bioelectronics,<sup>4</sup> wearable sensors,<sup>5</sup> stretchable energy-storage devices,<sup>6,7</sup> and flexible optoelectronic devices.<sup>8</sup> All of these applications require materials that are highly electrically conductive and mechanically compliant. One strategy to enable these functions is structurally designing the nonstretchable materials to absorb strain without fracture.<sup>9</sup> Alternatively, intrinsically stretchable conductive materials are highly desired, with intrinsic deformability and reliability at the forefront of concern. Some methods to achieve this include tailoring molecular structures or modifying morphologies of (semi-) conducting polymers,<sup>10,11</sup> incorporating conductive nano-fillers in stretchable networks,<sup>12</sup> or embedding liquid metals in elastomers.<sup>13</sup>

Stretchable conducting polymer-based hydrogels (SCPHs) with a three-dimensionally interconnected microstructure have presented attractive merits for use in energy-storage devices, biosensors, and medical electrodes.<sup>14</sup> The intrinsically porous structures found in hydrophilic gels have large surface areas that promote high water content, biocompatibility, and high permeability of ions and molecules.<sup>15</sup>

## Progress and Potential

Stretchable conductive materials play an important role in soft electronics. However, the disconnected nanoaggregates induced by phase instability and poor miscibility of components always restrict their mechanical and electrical properties. The present work controls the nano- and microstructure of stretchable conductive polymer-based hydrogels by using an ice-templated, low-temperature polymerization strategy. The obtained hierarchically structured stretchable conductive hydrogel shows significantly enhanced stretchability, conductivity, and electrochemical properties, which makes it a promising candidate for many applications, such as versatile strain sensors and stretchable supercapacitors.

Conducting polymers can be directly made into free-standing and flexible hydrogels by introducing multivalent metal ions<sup>3,16,17</sup> or via post-treatment with as-prepared polymers.<sup>18</sup> Despite their high electrical conductivity, the majority of conducting polymers lack stretchability (<10%) and possess limited mechanical compliance under large strains.

In an attempt to improve the stretchability, elastic polymer chains such as polyvinyl alcohol (PVA),<sup>19–21</sup> polyacrylamide (PAAm),<sup>22,23</sup> poly(ethylene glycol)diacrylate,<sup>4</sup> and chitosan<sup>24</sup> have been incorporated into rigid conducting polymers in past works. However, these strategies usually suffer from unfavorable electrical and mechanical properties. The introduction of nonconducting polymer chains in this case impedes the conductive pathways. Additionally, since the nucleation and reaction kinetics are controlled by the Gibbs free energy of nuclei formation, conventional polymerization in the liquid phase suffers from uncontrollable kinetics. The result is a random and loose assembly of disconnected, large polymeric nanoaggregates (Figure 1A, Morphology I), which lack a dense and continuous packing of conducting polymer chains and highly crystallized networks needed for both electron transport and robustness under tension.<sup>19,20,24</sup> Specifically, the limited amount of continuous conductive pathways cannot meet the percolation threshold, resulting in limited electrical and electrochemical properties when serving as electrodes or active materials in flexible electronics.<sup>20</sup> The loosely packed network is mechanically weak, with a typical tensile modulus of 10 kPa or less. When used as stretchable sensors in particular, their aggregates severely prohibit concurrent deformation along the bulk material upon stretching (Figure 1A, Morphology I), thus failing to reflect the actual strain with good fidelity, and ultimately leading to insufficient strain sensitivity.<sup>25</sup>

Here, we present an approach to create SCPs based on a conducting polymer-hydrogel interpenetrating double network with a hierarchical micro-/nanostructure, demonstrating enhanced mechanical, electrical, and electrochemical properties via high-performance strain sensors and supercapacitors (Figure 1A, Morphology II). Using ice-templating-assisted low-temperature polymerization (ITLP), the ice-templated gel (ItG) presents a hierarchical network by assembling interconnected, uniform nanofibrils to microsheets with a dendritic structure. The unique continuous dendrite micronetwork is created by ultra-low-temperature templating of high-hydrophilic solution, while the uniform nanofibrils are the result of low-temperature polymerization, which effectively suppress the undesirable aggregation.

Compared with conventional liquid-phase synthesized hydrogels (LpG), this multi-scale architecture has simultaneous drastic enhancements in performance, increasing 29 times and 83 times in its mechanical toughness and electrical conductivity, respectively. With the structural integrity and deformation adaptability at the nanoscale, the ItG, acting as a strain sensor, shows a broad linear detection range of strain (0%–107%) and high sensitivity (gauge factor  $\sim 1.4$ ). This is sufficient for the monitoring of several human daily functions, such as the heart's pulse, via small deformation, and joint motion via large deformation. Benefiting from the ordered assembly of nanofibrils into an interconnected micromesh, the ItG also serves as an electrode in a supercapacitor, with a specific capacitance of up to 888 F/g at 0.5 A/g, 2-fold higher than that obtained using LpG. The solid-state supercapacitors are then clearly demonstrated, showing an ultra-high area capacitance of 2,097 mF/cm<sup>2</sup> (368 A/g) and excellent deformation capability, such as bending, twisting, or stretching. The facile and universal design principle of stretchable conductive materials may provide unprecedented opportunities for broad applications in wearable electronics for energy storage and health monitoring.

<sup>1</sup>Department of Materials Science and Engineering, University of California, Los Angeles, Los Angeles, CA 90095, USA

<sup>2</sup>School of Materials Science and Engineering, Tsinghua University, Beijing 100084, P.R. China

<sup>3</sup>California Nanosystems Institute, Los Angeles, CA 90095, USA

<sup>4</sup>These authors contributed equally

<sup>5</sup>Lead Contact

\*Correspondence: [ximinhe@ucla.edu](mailto:ximinhe@ucla.edu)

<https://doi.org/10.1016/j.matt.2020.08.024>

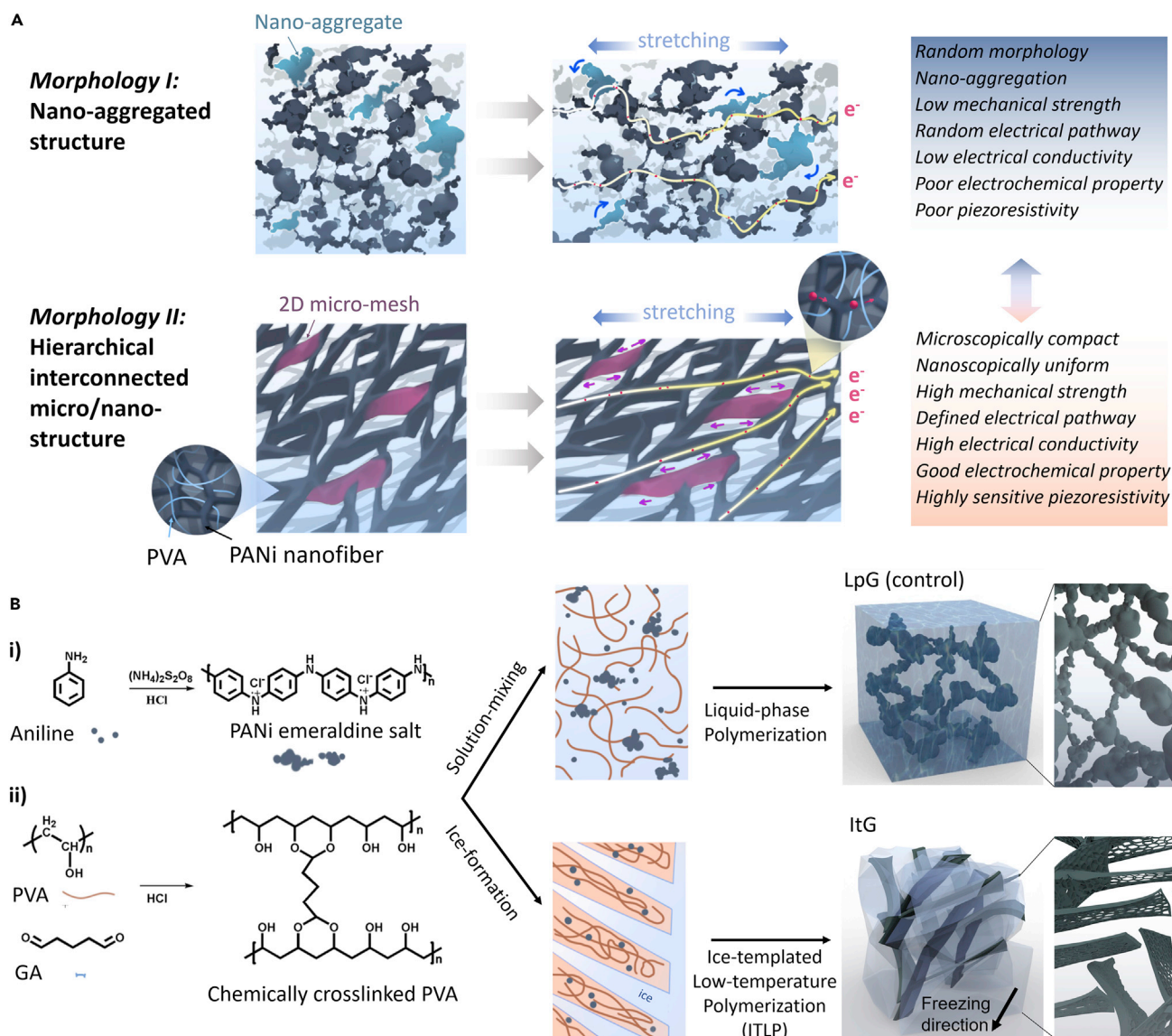


**Figure 1. Stretchable Conducting Polymer-Based Hydrogels with Enhanced Performance**

(A) Comparison of the morphologies and mechanisms of stretchable conducting polymer-based hydrogels (SCPHs) with the conductive components in, respectively, random disconnected nanoaggregates (upper, Morphology I, by conventional liquid-phase polymerization) and hierarchically interconnected micro-/nanostructure (lower, Morphology II, by ice-templated lower-temperature polymerization). Compared with the former, the latter possesses well-defined electron pathways for high electrical conduction. During stretching, the nanoaggregates (sky-blue region) in Morphology I are impeded from deforming in compliance with the bulk material deformation, whereas the synergic microscopic deformation (pink region) in the hierarchically structured Morphology II can conformably follow and more accurately reflect the macroscopic stretching of the gel, resulting in higher mechanical robustness and sensory capability.

(B) Preparation of PANi/PVA-based SCPHs by, respectively, traditional liquid-phase polymerization and ice-templated low-temperature polymerization, leading to Morphologies I and II in (A). The images of the ItG prepared by the ITLP method show the aligned dendrite microstructure formed with the ice template and the zoom-in view of the branches of the dendrites featuring nanoscale mesh structures.

See also [Figure S1](#).

## RESULTS AND DISCUSSION

### Materials Design and Synthesis

The ultimate goal is to create highly compact and interconnected conducting polymer chains intertwined with the stretchable polymer chains in a double network. We aim to mitigate the disconnected nanoaggregation, and instead create a

hierarchical structure across nanometer-to-millimeter scales continuously for enhanced mechanical, electrical, electrochemical, and piezoresistive sensing properties (Figure 1A, lower). Our method uniquely combines two key strategies: ice-templating and low-temperature polymerization.

Firstly, we propose to produce an interconnected, densely packed conducting polymer network by using ice as a template. As the ice is formed continuously through a temperature gradient, the polymer along the ice crystals also generates a well-defined continuous network.<sup>26</sup> In addition, the *in situ* ice growth expels the reactants along the ice crystals, which densifies the polymer chains into a tight packing and results in exceptional electrical and mechanical properties.<sup>27,28</sup> Secondly, polymerizing at low temperature is key to suppressing unintended nucleation. It has also been demonstrated that conducting polymers synthesized at low temperature possess higher crystallinity, fewer defects, and increased molecular weight, leading to a much greater electrical conductivity.<sup>29–31</sup>

This prior knowledge makes apparent the feasibility and compatibility of simultaneously ice-templating and low-temperature polymerizing both a hydrogel and a conducting polymer. To prove this concept, we used the ITLP technique to create a hierarchical and densified structure with less aggregation (Figure 1B, lower). Specifically, the reactant solution was first directionally frozen under a temperature gradient with liquid nitrogen ( $-196^{\circ}\text{C}$ ). Subsequently, the frozen sample was placed at low temperature ( $-20^{\circ}\text{C}$ ) for polymerization. For comparison, the control sample was fabricated through room-temperature liquid-phase polymerization (Figure 1B, upper).

As a representative SCPH, polyaniline (PANi)/PVA hydrogels were prepared by mixing two precursor solutions together and reacting them simultaneously (Figures 1B and S1). As such, aniline was polymerized in the presence of ammonium persulfate (APS), while PVA was chemically crosslinked by glutaraldehyde (GA), both in acidic conditions (Figure S2). The two polymers entangled and formed an interpenetrating network during the *in situ* reaction. Such a modular material design and fabrication procedure has been shown to be highly customizable and universal through our successful doping optimization and expansion to diverse polymer systems. Specifically, we optimized electrical conductivity of the SCPH by utilizing doping engineering, i.e., adding phytic acid (PA) into the precursor solution as the multivalent ionic molecule.<sup>16</sup> Furthermore, we extended this synthesis method to other stretchable conducting hydrogels (specifically PPy/PVA) and organogels, demonstrating broad applicability across different flexible electronics systems.

### Materials Characterization

The as-prepared PANi/PVA ItGs exhibited remarkable mechanical robustness (Figures 2A–2C), as they could be easily bent to  $180^{\circ}$ , stretched to 200% of their initial length, and knotted without breaking. Microscopically, the PANi/PVA ItG displayed a hierarchical structure that was highly ordered from microscale down to nanoscale (Figure 2Div–vi). Specifically, the ItG presented a distinct dendritic microstructure (Figure 2Div), constructed by connected two-dimensional microsheets (Figure 2Dv). Within each microsheet are nanofibrils woven into a porous mesh with high uniformity, where the conducting polymer PANi chains are evenly distributed and entangled with PVA chains (Figure 2Dvi). By contrast, the LpG synthesized under neither ice-templating nor low-temperature condition possessed irregularly shaped 100-nm-sized nanoagglomerates (Figure 2Di–iii) due to the unconfined overgrowth of polyaniline in the liquid phase.<sup>32</sup>

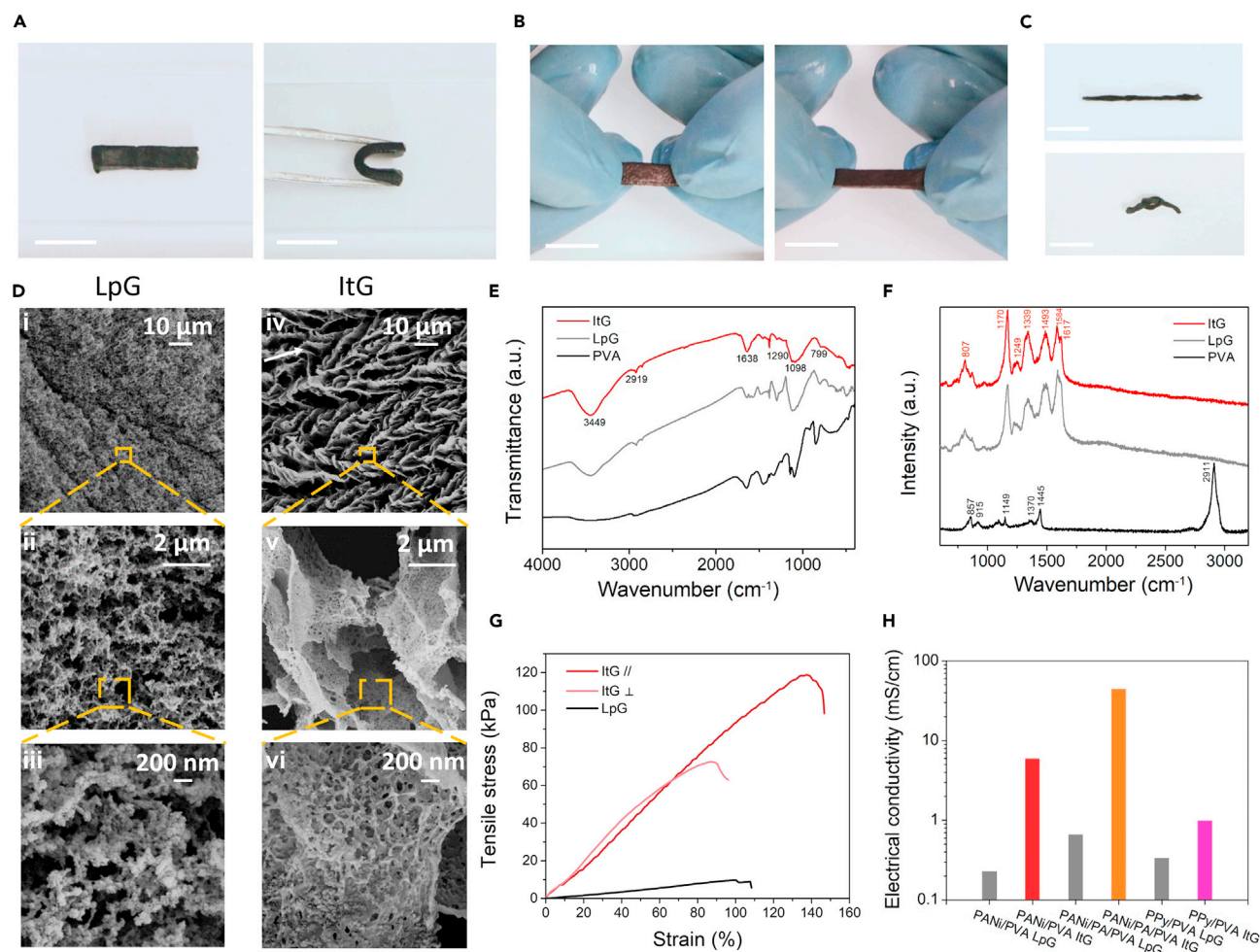


**Figure 2. Materials Characterization of ItG and LpG**

(A–C) Photographs of ItG show that the gel can be freely bent to 180° (A), stretched to 100% strain (B), and knotted (C). Scale bars, 1 cm.

(D) Scanning electron microscopy images of LpG (left) and ItG (right) at different magnifications. The white arrow in (iv) indicates the freezing direction.

(E) FTIR of ItG, LpG, and PVA in the wavenumber of 400 cm<sup>-1</sup> to 4,000 cm<sup>-1</sup>.

(F) Raman spectra of ItG, LpG, and PVA in the wavenumber of 600 cm<sup>-1</sup> to 3,200 cm<sup>-1</sup>.

(G) Stress-strain curves of ItG and LpG based on PANi/PA/PVA composites.

(H) Electrical conductivity of ItGs and LpGs based on PANi/PVA, PANi/PA/PVA, and PPy/PVA composites.

See also [Figures S3–S9](#) and [Table S1](#).

To investigate the structure formation mechanism, we also synthesized pure PANi (without PVA) to compare ITLP ([Figures S3A–S3C](#)) and room-temperature liquid-phase polymerization ([Figures S3D–S3F](#)), respectively. The ice-templated PANi presented typical oriented channels, confirming that the morphology of ItG is mainly controlled by directional ice formation; however, they did not exhibit the dendrite structure that PANi/PVA ItG displayed. This confirmed that the ice dendrite formation also relied on the presence of a hydrophilic component (PVA here, [Figure S3B](#)). On the other hand, the room-temperature, liquid-phase synthesized PANi exhibited neither oriented channels nor dendrite structures, instead showing a clustering structure similar to that of PANi/PVA LpG. This indicated that the nanoaggregates were attributed to the presence of PANi ([Figures S3D–S3F](#)).

Fundamentally, these comparisons reveal that such an elaborate hierarchical architecture of the ItG was the result of several mechanisms acting at different length

scales. Microscopically, the general morphology was mainly defined by the ice crystals as an effective template and could be easily removed simply by thawing. Typical natural ice has large vertical channels, but here a unique well-connected lamellar structure is formed. Such a structure resulted from the high hydrophilicity of PVA and its fast freezing rate (80–120  $\mu\text{m/s}$ ), which require minimum work to create critical ice nucleus and facilitate the constitutional supercooling of reactant solution.<sup>33</sup>

Nanoscopically, the ice crystals confined monomers and oxidant agents for aniline polymerization, which facilitated the directional polymerization<sup>29</sup> and also suppressed the growth of the large crystallites at the liquid-solid interface under ultra-low temperature,<sup>34</sup> leading to a nanofibril-connected network. Thermodynamically, the lower temperature ( $T$  in the equation below) resulted in the rise of activation energy ( $\Delta G$ )<sup>35</sup> and the decrease of the rate constant, and hence a controllable reaction kinetics of the polymer chain initiation and growth. These together led to less aggregation compared with room-temperature reaction.<sup>36</sup>

$$\Delta G^* = \frac{16\pi\gamma^3\nu^2}{3k_B T^2 \left(\ln \frac{C-C_0}{C_0}\right)^2},$$

where  $\Delta G^*$  is the Gibbs free energy for activation of nucleation,  $\gamma$  is the free energy increase per surface area,  $\nu$  is the volume of each nucleus,  $k_B$  is Boltzmann's constant,  $T$  is the temperature, and  $C_0$  and  $C$  are the saturation concentration and actual concentration of the reactants, respectively.

As an extension of this method, using the identical ITLP, PANi/PA/PVA, and PPy/PVA hydrogels all led to micro-/nanostructures similar to that of the PANi/PVA hydrogel (Figures S4 and S5). This demonstrates applicability to a wide variety of components of one's choosing, and also verifies the effectiveness of the unique, dendrite-shaped ice template and ultra-low-temperature condition to drive the formation of interconnected hierarchical structures for various compositions.

To examine whether there were any changes in polymer chemical structures due to the ice-templating process, we firstly characterized the PANi/PVA-based ItG and LpG with Fourier transform infrared (FTIR) spectroscopy and Raman spectroscopy (Figures 2E and 2F). In FTIR spectra, features at 1,638, 1,462, 1,390, 1,290, 1,098 and 899  $\text{cm}^{-1}$  confirmed that both gels contained typical PANi structures (Figure 2E).<sup>37</sup> The peaks at 3,449 and 2,919  $\text{cm}^{-1}$  were attributed to the O–H from intramolecular and intermolecular hydrogen bonds and alkyl groups in PVA.<sup>38</sup> Overall, the ItG and LpG presented identical peak positions according to the FTIR and Raman spectra. This indicated that PANi formed in both gels and there was no obvious difference between the chemical compositions of ItG and LpG. However, the X-ray diffraction (XRD) patterns showed that the ItG possessed a more prominent polyaniline peak compared with the LpG ( $2\theta = 26^\circ$ ), indicating that the ice-templated gel had substantial close packing of polymer chains with higher crystallinity (Figure S6), which may suggest their performance differences.

The mechanical properties of ItG and LpG were examined by tensile testing (Figure 2G and Table S1). The ItG was prepared by using a directional freezing process that created an anisotropic morphology, so we conducted stretching tests in both parallel and perpendicular to the alignment direction. Promisingly, the modulus and tensile strength of PANi/PA/PVA ItG parallel to the alignment direction (ItG//) were 119.8 kPa and 118.5 kPa, respectively, which were 12.0- and 12.3-fold higher than those of LpGs, demonstrating the effective strengthening in that direction.

More importantly, the toughness was improved to  $98.2 \text{ kJ/m}^3$  as well, increasing by 29-fold due to the ice-templating process. This simultaneous improvement indicates that the hierarchical architecture formed uniformly distributed stiff conducting and elastic hydrogel chains (Figure 1B)—in contrast to the disjointed aggregates seen in LpG (Figure 1A)—and can withstand larger forces while being stretched. In addition, the tensile strength and stretchability along the alignment direction were greater than those along the perpendicular direction (ItG  $\perp$ ), suggesting that the hydrogel network along the freezing direction had substantial structure integrity with less discontinuity (Figure 2Div). Similar strengthening and toughening effects also occurred in the PANi/PVA system, indicative of a general trend (Figure S7).

We measured the electrical conductivity of ItG and LpG using the AC impedance method (Figure S8).<sup>16</sup> The conductivity of PANi/PVA ItG along the alignment direction was about  $5.99 \text{ mS/cm}$ , in contrast to the  $0.23 \text{ mS/cm}$  of PANi/PVA LpG (Figure 2H). The structure modification of ItG presented a 26-fold electrical conductivity enhancement over LpG. After adding phytic acid as dopant, the conductivity of PANi/PA/PVA ItG along the alignment direction was further boosted to  $55.5 \text{ mS/cm}$ , 83-fold that for PANi/PA/PVA LpG. Using a 4-probe measurement, the conductivity of the ItG was  $91.0 \text{ mS/cm}$ . The conductivity of the PANi/PA/PVA ItG perpendicular to the alignment direction was slightly lower than in the parallel direction, presumably due to the increased structure discontinuity (Figure S9). Notably, this SCPH poses an electrical conductivity comparable with even a pure PANi hydrogel.<sup>16</sup> Similarly, we also measured the electrical conductivity of PPy/PVA gels, showing that ItG experienced a 3.0-fold enhancement relative to that of PPy/PVA LpG.

To investigate the mechanism behind the electrical conductivity improvement, we synthesized an LpG in liquid phase but at the same sub-zero temperature condition (by adding lithium chloride in the precursor solution to prevent ice formation). The as-prepared hydrogel demonstrated an electrical conductivity of  $\sim 0.45 \text{ mS/cm}$ , slightly higher than LpG but still one order of magnitude lower than ItG. This suggests that the low temperature for polymerization can indeed improve the electrical conductivity, possibly due to a higher molecular weight and crystallinity of conducting polymer.<sup>29</sup> The comparison between LpG and ItG indicates that the drastic conductivity increase of ItG predominantly arises from the hierarchical, interconnected micromesh structure induced by ice-templating; moreover, the volumetric expansion of the ice crystals would effectively concentrate the reactants into a further denser nanomesh that provides sufficient percolation of conducting polymer to conduct electrons.

### Sensing Applications

For stretchable and conductive materials fabricated by nanofiller and elastomer composites, the deformation of aggregated fillers is rather limited during stretching, leading to poor sensitivity (Figure 1A).<sup>25</sup> In addition, hydrogel sensors having inevitable ionic conduction suffer from inconsistent resistance changes over time under direct current (DC) due to the ion-derived migration and the formation of electric double layer. To overcome the aggregation and suppress the capacitance contribution under DC, we explored an ice-templated conductive organogel (ItOG) with uniformly distributed PANi and solvent exchange from water into ethylene glycol (EG).<sup>5</sup> The ItOG conductor maintained 100.26% of its initial resistance after 400 s, presenting ultra-high stability performance with pure electrical conduction behavior (Figure S10).

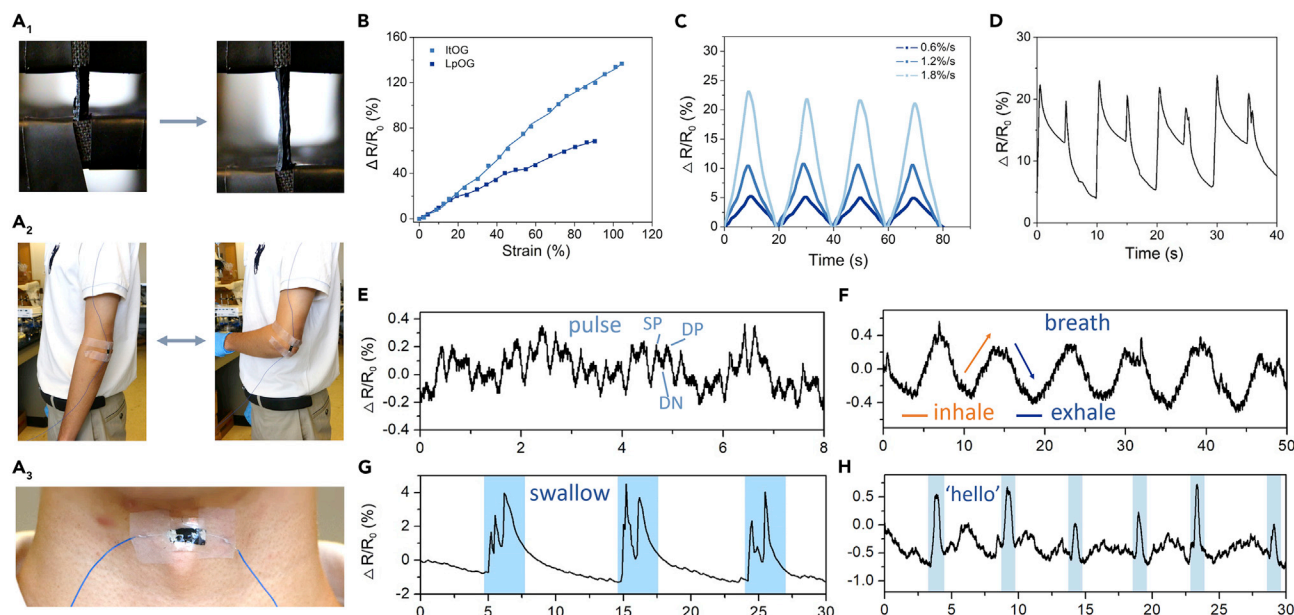


**Figure 3. Strain-Sensing Properties and Human Health Monitoring of PANi/PVA ItOG-Based Sensor**

(A<sub>1</sub>) Photos of ItOG during stretching to measure its strain sensitivity.

(A<sub>2</sub>) Human motion sensing by attaching an ItOG-based sensor on elbow.

(A<sub>3</sub>) Health monitoring by attaching an ItOG-based sensor on throat.

(B) Resistance change (%) upon stretching for PANi/PVA-based ItOG and LpOG.

(C) Strain response of ItOG under different stretching rates.

(D) Sensing of reversible bending and straightening of elbow motion by the sensor in (A<sub>2</sub>).

(E–H) Sensing of human pulse (E), breath (F), swallowing (G), and speaking (H) by the sensor in (A<sub>3</sub>) on the throat. SP, systolic peak; DN, diastolic notch; DP, diastolic peak.

See also [Figures S11](#) and [S12](#); [Video S1](#).

As the ItOG conductor was stretched while connected to a circuit to measure the resistance, the resistance displayed a continuous and linear increase as the strain increased ([Figures 3A<sub>1</sub>](#) and [3B](#)). The gauge factor ( $GF = \Delta R / (R_0 * \epsilon)$ ), defined as the ratio of relative resistance change to strain, was as large as 1.43, which is higher than poly(3,4-ethylenedioxythiophene) (PEDOT)/PVA and graphene/PAAm sensor at the corresponding stretching ratio.<sup>5,39</sup> The gauge factor of ItOG was 1.82 times relative to the liquid-phase synthesized organogel sensor (LpOG). The improved sensitivity is attributed to the mitigated nanoaggregation and thus the enhanced deformation adaptability. Under repetitive stretching and relaxing at strain rates ranging from 0.6%/s to 1.8%/s, the resistance changed periodically and rapidly, capable of reliable, real-time strain sensing ([Figure 3C](#)). The sensor had over 95% resistance retention after 500 cycles of stretching and recovery ([Figure S11](#)). Overall, the ItOG conductor showcased a large range of operation, desirable linearity, and high sensitivity and reversibility, as an ideal material for a high-performance strain sensor ([Figure S12](#)).

With such excellent sensing properties, we equipped the strain sensors to monitor human body movements.<sup>40</sup> We attached the polydimethylsiloxane (PDMS)-sealed ItOG to a human elbow ([Figure 3A<sub>2</sub>](#)), and the sensor easily conformed to the skin surface—a result of ItOG's high stretchability, high flexibility, and light weight.<sup>41</sup> We monitored the change in resistance of the sensor during instant bending and gradual straightening of the elbow, presenting well-defined sensitivity and reliability ([Figure 3D](#) and [Video S1](#)).

Furthermore, we examined the sensing performance for recognizing small-scale human motion by attaching the sensor to a human throat (Figure 3A<sub>3</sub>). Since the intensity and shape of the signal varied with different motions, we can identify the different motions from the characteristic readout signals of the sensor. Particularly, the heart rate of the human is precisely read by the adjacent lower limit, calculated to be approximately 96 beats per minute. During one typical waveform of a heart-beat, the systolic peak, dicrotic notch, and diastolic peak were accurately identified (Figure 3E).<sup>42</sup> In addition, the sensor could clearly detect respiratory signals during each inhalation-exhalation cycle, swallowing, and speaking according to the characteristic pattern and intensity of each movement (Figures 3F–3H). Overall, combined with the broad sensing range, linearity, and sensitivity, the ItOG strain sensor can simultaneously monitor multiple daily activities of humans with both small and large strain windows.

### Electrochemical Applications

With the remarkable conductivity enhancement of the ItG, we then studied the electrochemical properties for energy-storage applications. Particularly, we used cyclic voltammetry (CV), galvanostatic charge-discharge (GCD), and electrochemical impedance spectroscopy (EIS) to characterize ItG and LpG as supercapacitor electrodes in a standard three-electrode system. For simplification, we denoted the PANi/PVA system as PP and the PANi/PA/PVA system as PPP. The comparison of CV at a scan rate of 10 mV/s is presented in Figure 4A. The two pairs of PANi redox peaks are clearly observed both for ItG and LpG, indicating the pseudocapacitor mechanism. The enclosed CV area suggests that the specific capacitance of ItG electrode was larger than that of LpG electrode. Figure 4B presents the Nyquist plots of ItG and LpG electrodes. The reduction of equivalent series resistance (ESR) was obtained, indicating the improved electrical transfer in the ItG electrode. The GCD curves of PPP ItG and PP ItG at a current density of 2 A/g had significantly longer discharging time compared with those of PPP LpG and PP LpG, shown by Figure 4C. Accordingly, the specific capacitances of the four samples ranging from 0.5 A/g to 20 A/g were calculated (Figure 4D). The specific capacitance of ItG was considerably higher than that of LpG. Notably, the specific capacitance of PPP ItG reached 888 F/g at 0.5 A/g, which was superior to LpG electrodes (431 F/g for PPP Ft and 295 F/g for PP Ft) and PANi-based electrodes in the literature (59.1–480 F/g).<sup>16,43–47</sup> The improvement in capacitance and thus energy/power density (Figure 4E) for ItG is attributed to the lower ESR and thus lower energy loss during charging and discharging. The PP ItG and PPP ItG also had a capacitance retention of 90% and 86%, respectively, after 1,000 charging-discharging cycles, indicating the materials' good cyclic stability (Figure 4F). To further generalize the method, we also investigated PPy/PVA (Figure S13) as electrodes. The GCD and CV results all verified the significant improvement in electrochemical performance by using this strategy. The enhancement of the overall electrochemical property is due to the interconnected conduction pathway across nano- and microscales for high electrical conductivity and the reduced energy loss.

The hierarchical micro-to-nanostructured hydrogel created from this method is a strong contender for practical application in electrochemical devices. Accordingly, we used the PPP ItG as an electrode material for a solid-state supercapacitor (SSC). The areal loading of PANi after pressing was calculated as 5.7 mg/cm<sup>2</sup>. To make the device, we sandwiched a PVA/H<sub>3</sub>PO<sub>4</sub> film and a cellulose-based separator between two PPP ItG films, before pressing them and then drying them in air.

The Nyquist plots in Figure 5A show that the ESR was 5.21 Ω/cm<sup>2</sup> and charge-transfer resistance ( $R_{CT}$ ) was 0.13 Ω/cm<sup>2</sup>, which are very low for a flexible SSC device. In addition,

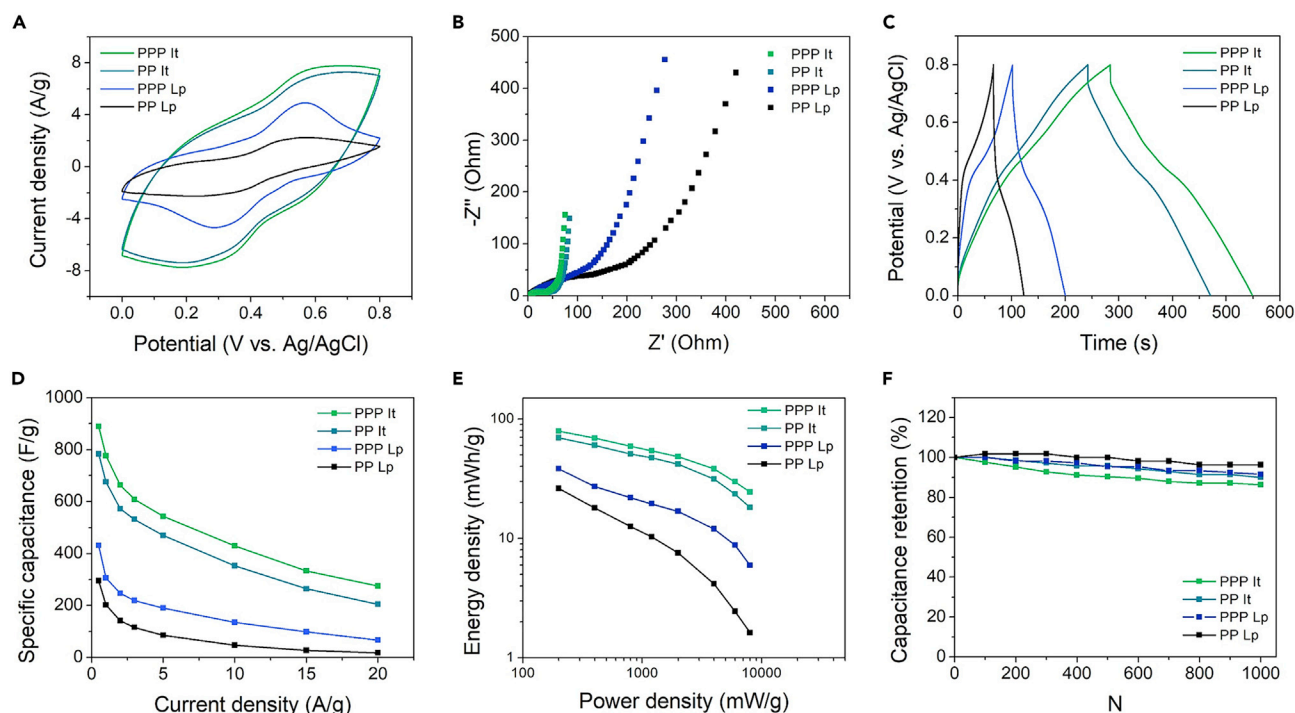


**Figure 4. Electrochemical Properties of ItG and LpG based on PANi/PVA (PP) and PANi/PA/PVA (PPP)**

(A) CV curves at a scan rate of 10 mV/s.

(B) EIS in the frequency range of 10,000–0.01 Hz.

(C) GCD at a current density of 2 A/g.

(D) Specific capacitance at current densities of 0.5–20 A/g.

(E) Ragone plot of electrodes.

(F) Capacitance retention after 1,000 charging-discharging cycles at a current density of 10 A/g.

See also [Figure S13](#).

the nearly vertical line at the low-frequency region indicated an ideal capacitive behavior of the ItG electrode. The CV curves at different scan rates (5–100 mV/s) showed similar symmetric shape ([Figure 5B](#)), indicating good capacitive behavior of the ItG electrode. The charge-discharge curves at different current densities (2–30 mA/cm<sup>2</sup>, much higher than in the literature with a current density of 0.01–1 mA/cm<sup>2</sup>), demonstrated a remarkable performance featuring a small potential drop (iR drop) at the beginning of the discharging and symmetric triangular shapes ([Figure 5C](#)). The areal capacitance of the device calculated from the GCD data ([Figure 5D](#)) could reach 2,097 mF/cm<sup>2</sup> with the specific capacitance of 367 F/g at the current density of 2 mA/cm<sup>2</sup>. Meanwhile, the Coulombic efficiency was >95% covering the entire current density range. Notably the device, under such a high mass loading, still exhibited 65% capacitance retention even at an extremely high current density of 20 mA/cm<sup>2</sup>, which is regarded as an excellent rate capability for devices with ultra-high capacitance.<sup>21,48</sup> The relatively small capacitance decrease observed at high current density arises from the good conductivity of the electrode, which reduces the iR drops. Through calculation based on the capacitance data, the SSC demonstrated a maximum energy density of 186  $\mu$ Wh/cm<sup>2</sup> at a power density of 1,600  $\mu$ W/cm<sup>2</sup> and maintained 95  $\mu$ Wh/cm<sup>2</sup> at a power density of 24,000  $\mu$ W/cm<sup>2</sup>. The areal capacitance, energy density, and power density of the SSC were among the best in comparison with the previous SSC reports ([Figures S14 and 5E](#); [Table S2](#)). The device also performed 87.7% capacitance retention and nearly 100% Coulombic efficiency after 2,000 reversible charging-discharging cycles, suggesting excellent cyclic stability of the SSC device ([Figure 5F](#)). For comparison, we also

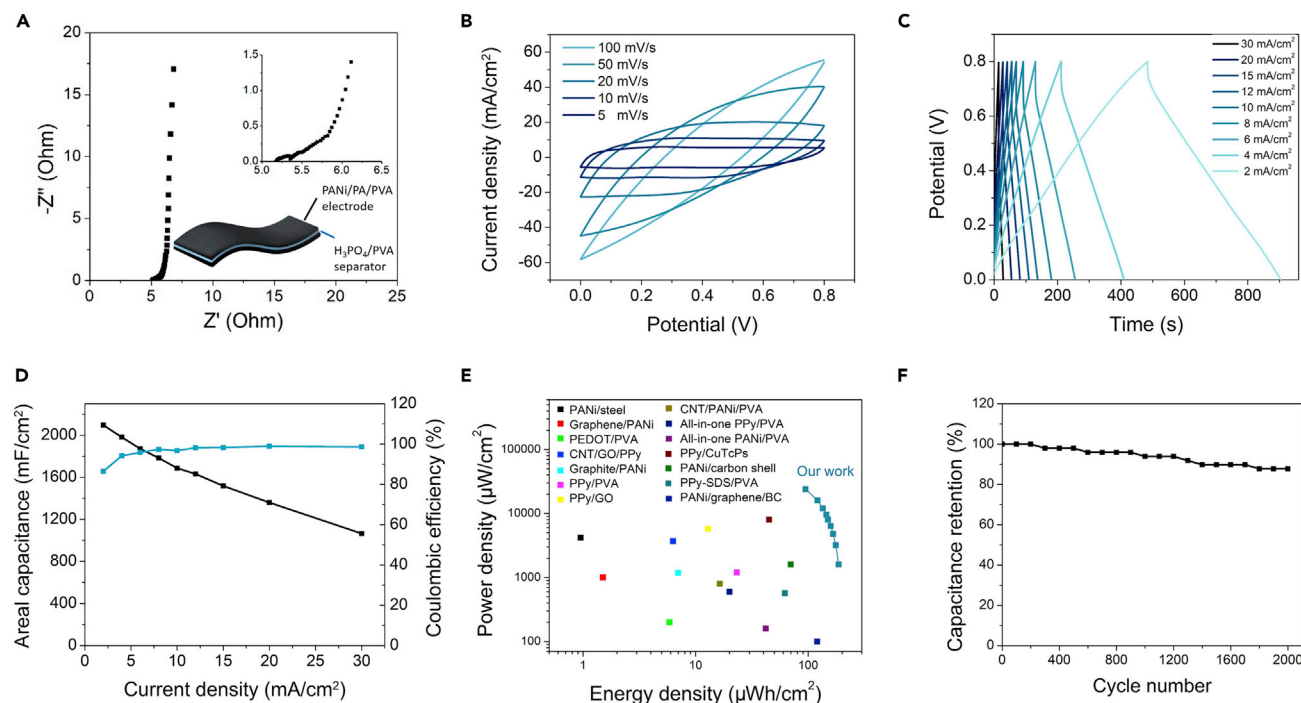


**Figure 5. Electrochemical Characterization of Solid-State Supercapacitors**

(A) EIS curve in the range of 10,000–0.01 Hz.

(B) CV curves at scan rates of 5–100 mV/s.

(C) GCD curves at current densities of 2–30 mA/cm<sup>2</sup>.

(D) Areal capacitance and Coulombic efficiency calculated from the GCD data.

(E) Ragone plot of power density and energy density in comparison with literature.

(F) Capacitance retention (87.3%) of the SSC over 2,000 charging-discharging cycles.

See also [Figures S14](#) and [S15](#); [Table S2](#).

characterized the SSC with PP ItG electrodes, as shown in [Figure S15](#). The areal capacitance was calculated to be 1,786 mF/cm<sup>2</sup> (247 F/g) at a current density of 2 mA/cm<sup>2</sup>, and the capacitance retention was at 79% after 2,000 cycles of reversible charging/discharging.

Given its promising performance and mechanical softness, we also investigated the ItG's potential for flexible and stretchable electronics applications. During and after bending our devices from 0° to 180° and twisting from 0° to 90°, the CV and GCD curves showed little variance from static samples ([Figures S16](#) and [S17](#)). Accordingly, the capacitance and Coulombic efficiency calculated from the GCD curves are well retained ([Figures 6A](#) and [6B](#)). After 2,000 cycles of 90° bending, over 97% of the capacitance retention remained, illustrating excellent bending stability ([Figure 6C](#)). A stretchable supercapacitor was also fabricated by using a physically crosslinked PVA film as a separator. The device could retain 74% capacitance under 80% uniaxial strain, suggesting potential use for stretchable electronics ([Figures 6D](#) and [6E](#)).

As a proof of concept, we have further demonstrated SCPH in wearable applications. Three SSCs connected in series, after charging, could light up a red light-emitting diode (LED) for more than 5 min. With rigorous bending and twisting of each supercapacitor, the red LED remained lit without any obvious decline in light intensity ([Figure 6F](#)). Additionally, the device that was wrapped around the arm operated well during regular arm motion ([Figure 6G](#) and [Video S2](#)).

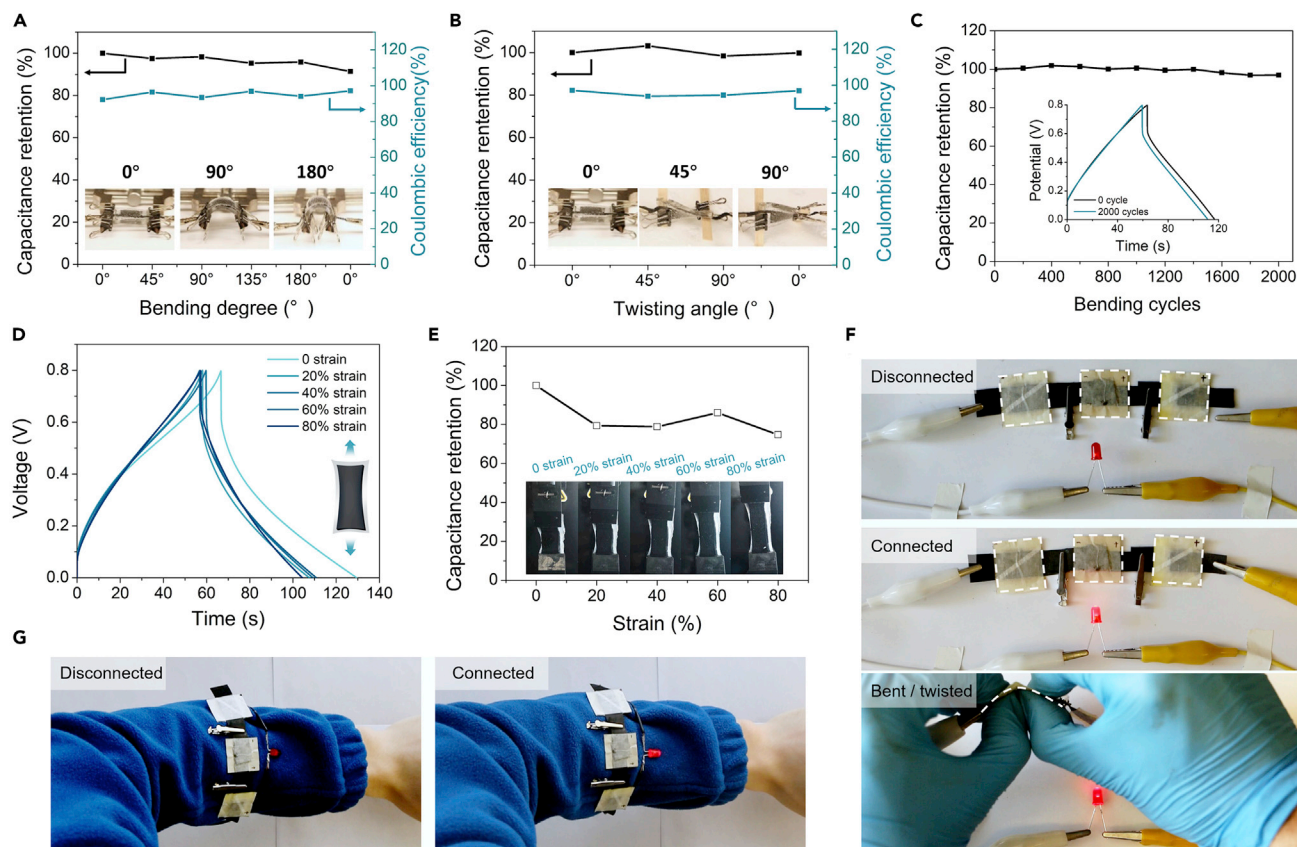


**Figure 6. Demonstrations of Flexible and Stretchable Supercapacitors as Wearable Electronics**

(A and B) Capacitance retention and Coulombic efficiency of SSC under various bending angles (A) and twisting angles (B).

(C) Capacitance retention (97%) of SSC over 2,000 bending/unbending cycles.

(D) Galvanostatic charge-discharge (GCD) curves of the stretchable SSC under stretching at various strains (0%–80%).

(E) Capacitance retention of the stretchable SSC under various strains (0%–80%).

(F) Three SSCs connected in series to light up a red LED. The device withstood manual bending and twisting without obvious performance deterioration.

(G) Wearable demonstration of three connected SSCs that wrap around a human arm functioning well during regular arm motion.

See also [Figures S16](#) and [S17](#); [Video S2](#).

## Conclusions

This work demonstrates a novel method of ice-template-assisted low-temperature polymerization to synthesize SCPH with a hierarchical architecture composed of a dense, interconnected, nanofiber micronetwork. Unlike the aggregation widely observed as a consequence of composite fabrication, the uniform and mesh-like distribution of conducting polymer in the elastic networks provides enhanced mechanical robustness and a well-defined and continuous electrical conduction pathway. Utilized as strain sensors, the conducting hydrogels with less-aggregated structures can accurately capture minute mechanical deformation by transducing it into piezoresistive signals. In particular, human motions of both large and small strains can be monitored in real time, demonstrating outstanding broad-range sensory capabilities. Thanks to the continuous highway it provides for electron and ion transportation, the electrochemical performance of the materials being used in the three-electrode system and solid-state supercapacitors is greatly improved. The strategy can be generalized to broad choices of materials systems, such as polypyrrole and PEDOT. Overall, this facile and universal synthesis method has well addressed some long-lasting challenges in the field of intrinsically stretchable conductive materials, provides a methodology to create a hierarchical, uniform nano-/microstructure,

and can further facilitate the development of mechanically compliant electronic devices, especially as it may pertain to energy-storage and sensory systems—biological and industrial alike.

## EXPERIMENTAL PROCEDURES

### Resource Availability

#### Lead Contact

Further information and requests for resources and reagents should be directed to and will be fulfilled by the Lead Contact, Ximin He ([ximinhe@ucla.edu](mailto:ximinhe@ucla.edu))

#### Materials Availability

This study did not generate new unique reagents. PVA (molecular weight = 89,000–98,000, hydrolysis degree = 99%), aniline, pyrrole, and PA (50 wt % aqueous solution) were purchased from Sigma. Aniline was purified by reduced distillation. Lithium chloride, GA (50% aqueous solution), and APS (ACS grade) were purchased from Fisher. Sylgard 184 Silicone Elastomer kits were purchased from Ellsworth.

#### Data and Code Availability

All data needed to evaluate the conclusions in the paper are present in the paper and/or [Supplemental Information](#). Additional data related to this paper may be requested from the authors.

### Synthesis of PANi/PVA and PANi/PA/PVA SCPHs

PVA solution (10 wt %) was prepared by adding PVA in deionized (DI) water and heated to 85°C. The solution was cooled and stored for further usage. For the synthesis of PANi/PVA hydrogel composites, 2,000 mg of 10 wt % PVA solution, 147  $\mu$ L of purified aniline, and 285  $\mu$ L of 35.5% HCl solution was mixed together to form 3 mL of aqueous solution in total, denoted as solution A. For the synthesis of PANi/PA/PVA gel, an additional 296  $\mu$ L of 50 wt % PA solution was added into solution A. Solution B was made by mixing 0.4 mL of 1 wt % GA and 365 mg APS together to form 1 mL of aqueous solution. The solutions were cooled to 4°C and mixed in a water/ice bath.

The ItG was made by freezing the precursor mixture in a 3D-printed mold above a tank of liquid nitrogen. After entire freezing, the sample was quickly transferred to a –20°C fridge for a sub-zero-temperature reaction. The mixture was then melted to obtain the ItG. The liquid-phase polymerized gel (LpG) was cured at room temperature and kept in the –20°C fridge, and melted at room temperature.

### Fabrication of Solid-State Supercapacitors

Two pieces of as-prepared ItG films soaked in 4 M LiCl solution were compressed to form two electrodes. A PVA-H<sub>3</sub>PO<sub>4</sub> gel separator was sandwiched between the two ItG electrodes with a cellulose-based separator in between. The flexible supercapacitor was encapsulated in a PDMS mode or tape with the ends of carbon cloth overhanging out for connection. The stretchable supercapacitor was made by using the physically crosslinked PVA film as a separator and conducting reversible freeze-thawing to combine the three layers together.

### Fabrication of ItOG-Based Strain Sensor

The ItOG was made in the form of thin film and immersed in EG for 2 days. For strain sensor application, the as-prepared ItOG was connected to two silver wires using silver paste and subsequently covered by a thin layer of PDMS precursor solution (10:1 weight ratio of Sylgard 184 Silicone Elastomer). The film with PDMS precursor was kept in a 50°C oven for 2 h to complete the PDMS polymerization.

### Characterizations

The morphologies of samples were examined with Supra 40VP scanning electron microscope. The chemical compositions were analyzed with FTIR spectroscopy and Raman spectroscopy. The strain-stress curves of the gel samples were measured by a dynamic mechanical analyzer. The electrical conductivity of SCPHs was measured both by impedance using alternating current and 4-probe measurement using direct current. The electrochemical properties were characterized by a CHI660E electrochemical workstation. The tests of electrodes were conducted in 1 M H<sub>2</sub>SO<sub>4</sub> aqueous solution in a three-electrode system. The tests of SSC were conducted in a two-electrode system with two pieces of carbon cloth as current collectors. Strain sensing of elbow and throat was done by attaching the device directly to the workstation and the current was detected using i-t mode. The resistance was calculated based on current data in real time.

### SUPPLEMENTAL INFORMATION

Supplemental Information can be found online at <https://doi.org/10.1016/j.matt.2020.08.024>.

### ACKNOWLEDGMENTS

The research was supported by the NSF award 1724526, the ONR award N000141712117, the ONR award N00014-18-1-2314, the AFOSR grant FA9550-17-1-0311, and the AFOSR award FA9550-18-1-0449. The authors thank Jin Cai for help with the XRD experiment.

### AUTHOR CONTRIBUTIONS

Conceptualization, X.H.; Methodology, X.H., Y. Zhao, and B.Z.; Investigation, X.H., Y. Zhao, B.Z., B.Y., Y.Q., Z.P., and Y. Zhang; Writing – Original Draft, X.H., Y. Zhao, and B.Z.; Writing – Review & Editing, Y. Zhao, B.Z., Y.A., I.F., K.Y., Q.P., and X.H.; Funding Acquisition, X.H.; Resources, Q.P. and X.H.; Supervision, X.H.

### DECLARATION OF INTERESTS

The authors declare no competing interests.

Received: May 14, 2020

Revised: July 10, 2020

Accepted: August 19, 2020

Published: September 17, 2020

### REFERENCES

- Yang, J.C., Mun, J., Kwon, S.Y., Park, S., Bao, Z., and Park, S. (2019). Electronic skin: recent progress and future prospects for skin-attachable devices for health monitoring, robotics, and prosthetics. *Adv. Mater.* *31*, 1904765.
- Son, D., Lee, J., Qiao, S., Ghaffari, R., Kim, J., Lee, J.E., Song, C., Kim, S.J., Lee, D.J., and Jun, S.W. (2014). Multifunctional wearable devices for diagnosis and therapy of movement disorders. *Nat. Nanotechnol.* *9*, 397.
- Feig, V.R., Tran, H., Lee, M., Liu, K., Huang, Z., Beker, L., Mackanic, D.G., and Bao, Z. (2019). An electrochemical gelation method for patterning conductive PEDOT:PSS hydrogels. *Adv. Mater.* *31*, e1902869.
- Guarino, V., Alvarez-Perez, M.A., Borriello, A., Napolitano, T., and Ambrosio, L. (2013). Conductive PANi/PEGDA macroporous hydrogels for nerve regeneration. *Adv. Healthc. Mater.* *2*, 218–227.
- Lee, Y.Y., Kang, H.Y., Gwon, S.H., Choi, G.M., Lim, S.M., Sun, J.Y., and Joo, Y.C. (2016). A strain-insensitive stretchable electronic conductor: PEDOT:PSS/acrylamide organogels. *Adv. Mater.* *28*, 1636–1643.
- Zhao, F., Bae, J., Zhou, X., Guo, Y., and Yu, G. (2018). Nanostructured functional hydrogels as an emerging platform for advanced energy technologies. *Adv. Mater.* *30*, e1801796.
- Li, L., Lou, Z., Chen, D., Jiang, K., Han, W., and Shen, G. (2018). Recent advances in flexible/stretchable supercapacitors for wearable electronics. *Small* *14*, 1702829.
- Yin, D., Jiang, N.R., Chen, Z.Y., Liu, Y.F., Bi, Y.G., Zhang, X.L., Feng, J., and Sun, H.B. (2019). Roller-assisted adhesion imprinting for high-throughput manufacturing of wearable and stretchable organic light-emitting devices. *Adv. Opt. Mater.* *8*, 1901525.
- Wang, C., Wang, C., Huang, Z., and Xu, S. (2018). Materials and structures toward soft electronics. *Adv. Mater.* *30*, 1801368.
- O'Connor, B., Chan, E.P., Chan, C., Conrad, B.R., Richter, L.J., Kline, R.J., Heeney, M., McCulloch, I., Soles, C.L., and DeLongchamp, D.M. (2010). Correlations between mechanical

- and electrical properties of polythiophenes. *ACS Nano* 4, 7538–7544.
11. Wang, Y., Zhu, C., Pfattner, R., Yan, H., Jin, L., Chen, S., Molina-Lopez, F., Lissel, F., Liu, J., and Rabiah, N.I. (2017). A highly stretchable, transparent, and conductive polymer. *Sci. Adv.* 3, e1602076.
  12. Sekitani, T., Noguchi, Y., Hata, K., Fukushima, T., Aida, T., and Someya, T. (2008). A rubberlike stretchable active matrix using elastic conductors. *Science* 321, 1468–1472.
  13. Dickey, M.D. (2017). Stretchable and soft electronics using liquid metals. *Adv. Mater.* 29, 1606425.
  14. Han, Y., and Dai, L. (2019). Conducting polymers for flexible supercapacitors. *Macromolecular Chem. Phys.* 220, 1800355.
  15. Ghosh, S., and Inganäs, O. (1999). Conducting polymer hydrogels as 3D electrodes: applications for supercapacitors. *Adv. Mater.* 11, 1214–1218.
  16. Pan, L., Yu, G., Zhai, D., Lee, H.R., Zhao, W., Liu, N., Wang, H., Tee, B.C., Shi, Y., Cui, Y., et al. (2012). Hierarchical nanostructured conducting polymer hydrogel with high electrochemical activity. *Proc. Natl. Acad. Sci. U S A* 109, 9287–9292.
  17. Wang, Y., Shi, Y., Pan, L., Ding, Y., Zhao, Y., Li, Y., Shi, Y., and Yu, G. (2015). Dopant-enabled supramolecular approach for controlled synthesis of nanostructured conductive polymer hydrogels. *Nano Lett.* 15, 7736–7741.
  18. Yao, B., Wang, H., Zhou, Q., Wu, M., Zhang, M., Li, C., and Shi, G. (2017). Ultrahigh-conductivity polymer hydrogels with arbitrary structures. *Adv. Mater.* 29, 1700974.
  19. Li, W., Gao, F., Wang, X., Zhang, N., and Ma, M. (2016). Strong and robust polyaniline-based supramolecular hydrogels for flexible supercapacitors. *Angew. Chem. Int. Ed.* 55, 9196–9201.
  20. Huang, H., Yao, J., Li, L., Zhu, F., Liu, Z., Zeng, X., Yu, X., and Huang, Z. (2016). Reinforced polyaniline/polyvinyl alcohol conducting hydrogel from a freezing–thawing method as self-supported electrode for supercapacitors. *J. Mater. Sci.* 51, 8728–8736.
  21. Chen, F., Chen, Q., Song, Q., Lu, H., and Ma, M. (2019). Strong and stretchable polypyrrole hydrogels with biphasic microstructure as electrodes for substrate-free stretchable supercapacitors. *Adv. Mater. Inter.* 6, 1900133.
  22. Tang, Q., Wu, J., Sun, H., Fan, S., Hu, D., and Lin, J. (2008). Superabsorbent conducting hydrogel from poly (acrylamide-aniline) with thermo-sensitivity and release properties. *Carbohydr. Polym.* 73, 473–481.
  23. Dai, T., Qing, X., Zhou, H., Shen, C., Wang, J., and Lu, Y. (2010). Mechanically strong conducting hydrogels with special double-network structure. *Synth. Met.* 160, 791–796.
  24. Huang, H., Wu, J., Lin, X., Li, L., Shang, S., Yuen, M.C.-w., and Yan, G.J.C.p. (2013). Self-assembly of polypyrrole/chitosan composite hydrogels. *Carbohydr. Polym.* 95, 72–76.
  25. Lei, Z., and Wu, P. (2019). A highly transparent and ultra-stretchable conductor with stable conductivity during large deformation. *Nat. Commun.* 10, 3429.
  26. Zhao, Y., Alsaïd, Y., Yao, B., Zhang, Y., Zhang, B., Bhuskute, N., Wu, S., and He, X. (2020). Wood-inspired morphologically tunable aligned hydrogel for high-performance flexible all-solid-state supercapacitors. *Adv. Funct. Mater.* 30, 1909133.
  27. Wu, S., Zhu, C., He, Z., Xue, H., Fan, Q., Song, Y., Francisco, J.S., Zeng, X.C., and Wang, J. (2017). Ion-specific ice recrystallization provides a facile approach for the fabrication of porous materials. *Nat. Commun.* 8, 15154.
  28. Lu, J., Wang, H., Tian, Z., Hou, Y., and Lu, H. (2020). Cryopolymerization of 1, 2-dithiolanes for the facile and reversible grafting-from synthesis of protein-polydisulfide conjugates. *J. Am. Chem. Soc.* 142, 1217–1221.
  29. Maity, P.C., and Khandelwal, M. (2016). Synthesis time and temperature effect on polyaniline morphology and conductivity. *Am. J. Mater. Synth. Process.* 1, 37.
  30. Adams, P., Laughlin, P., Monkman, A., and Kenwright, A. (1996). Low temperature synthesis of high molecular weight polyaniline. *Polymer* 37, 3411–3417.
  31. Adams, P., and Monkman, A. (1997). Characterization of high molecular weight polyaniline synthesized at -40° C using a 0.25:1 mole ratio of persulfate oxidant to aniline. *Synth. met.* 87, 165–169.
  32. Li, W., Lu, H., Zhang, N., and Ma, M. (2017). Enhancing the properties of conductive polymer hydrogels by freeze-thaw cycles for high-performance flexible supercapacitors. *ACS Appl. Mater. Interfaces* 9, 20142–20149.
  33. Zhang, H., Hussain, I., Brust, M., Butler, M.F., Rannard, S.P., and Cooper, A.I. (2005). Aligned two- and three-dimensional structures by directional freezing of polymers and nanoparticles. *Nat. Mater.* 4, 787–793.
  34. Huang, J., and Kaner, R.B. (2006). The intrinsic nanofibrillar morphology of polyaniline. *Chem. Commun.* 4, 367–376.
  35. Wei, H., Huang, K., Zhang, L., Ge, B., Wang, D., Lang, J., Ma, J., Wang, D., Zhang, S., and Li, Q. (2018). Ice melting to release reactants in solution syntheses. *Angew. Chem. Int. Ed.* 130, 3412–3417.
  36. Pincock, R.E. (1969). Reactions in frozen systems. *Acc. Chem. Res.* 2, 97–103.
  37. Ghebache, Z., Hamidouche, F., Safidine, Z., Trari, M., and Bellal, B. (2019). Synthesis and electrical conducting properties of poly(aniline) doped with zeolite HY nanocomposites containing SnO<sub>2</sub> for high-performance supercapacitor electrode. *J. Inorg. Organomet. Polym. Mater.* 29, 1548–1558.
  38. Mansur, H.S., Sadahira, C.M., Souza, A.N., and Mansur, A.A. (2008). FTIR spectroscopy characterization of poly(vinyl alcohol) hydrogel with different hydrolysis degree and chemically crosslinked with glutaraldehyde. *Mater. Sci. Eng. C* 28, 539–548.
  39. Zhang, H., Niu, W., and Zhang, S. (2018). Extremely stretchable, stable, and durable strain sensors based on double-network organogels. *ACS Appl. Mater. Inter.* 10, 32640–32648.
  40. Zhang, S.-H., Wang, F.-X., Li, J.-J., Peng, H.-D., Yan, J.-H., and Pan, G.-B. (2017). Wearable wide-range strain sensors based on ionic liquids and monitoring of human activities. *Sensors* 17, 2621.
  41. Hattori, Y., Falgout, L., Lee, W., Jung, S.Y., Poon, E., Lee, J.W., Na, I., Geisler, A., Sadhwani, D., and Zhang, Y. (2014). Multifunctional skin-like electronics for quantitative, clinical monitoring of cutaneous wound healing. *Adv. Healthc. Mater.* 3, 1597–1607.
  42. Yang, T., Jiang, X., Zhong, Y., Zhao, X., Lin, S., Li, J., Li, X., Xu, J., Li, Z., and Zhu, H. (2017). A wearable and highly sensitive graphene strain sensor for precise home-based pulse wave monitoring. *ACS Sensors* 2, 967–974.
  43. Li, H., Lv, T., Li, N., Yao, Y., Liu, K., and Chen, T. (2017). Ultraflexible and tailorable all-solid-state supercapacitors using polyacrylamide-based hydrogel electrolyte with high ionic conductivity. *Nanoscale* 9, 18474–18481.
  44. Li, P., Jin, Z., Peng, L., Zhao, F., Xiao, D., Jin, Y., and Yu, G. (2018). Stretchable all-gel-state fiber-shaped supercapacitors enabled by macromolecularly interconnected 3D graphene/nanostructured conductive polymer hydrogels. *Adv. Mater.* 30, 1800124.
  45. Liu, R., Ma, L., Huang, S., Mei, J., Xu, J., and Yuan, G. (2017). A flexible polyaniline/graphene/bacterial cellulose supercapacitor electrode. *New J. Chem.* 41, 857–864.
  46. Yu, J., Lu, W., Pei, S., Gong, K., Wang, L., Meng, L., Huang, Y., Smith, J.P., Booksh, K.S., and Li, Q. (2016). Omnidirectionally stretchable high-performance supercapacitor based on isotropic buckled carbon nanotube films. *ACS Nano* 10, 5204–5211.
  47. Zang, X., Li, X., Zhu, M., Li, X., Zhen, Z., He, Y., Wang, K., Wei, J., Kang, F., and Zhu, H. (2015). Graphene/polyaniline woven fabric composite films as flexible supercapacitor electrodes. *Nanoscale* 7, 7318–7322.
  48. Chen, C., Zhang, Y., Li, Y., Dai, J., Song, J., Yao, Y., Gong, Y., Kierzewski, I., Xie, J., and Hu, L. (2017). All-wood, low tortuosity, aqueous, biodegradable supercapacitors with ultra-high capacitance. *Energy Environ. Sci.* 10, 538–545.